Experimental Investigation on Ice Accretion Upon Ice Particle Impacting onto Heated Surface

Haiyang Hu,* Linchuan Tian,† and Hui Hu‡
Iowa State University, Ames, Iowa 50011

An experimental study was conducted to examine the dynamic ice accretion process upon the impingement of microsized, airborne ice particles/crystals onto a heated test surface pertinent to aeroengine icing phenomena. The experimental study was conducted in a specially designed ice crystal icing test facility to generate and inject microsized ice particles into a frozen-cold airflow. The microsized ice particles were forced to impinge onto a heated test plate with controllable surface temperatures. Upon impingement of the ice particles onto the heated test surface, the dynamic ice accretion process was found to take place over the heated surface in three distinct stages: 1) an ice-melting stage at the beginning, followed by 2) an ice/water mixture formation stage, and then 3) a water refreezing stage, causing the formation of a solid ice layer accreted on the heated test surface eventually. After impinging onto the test plate, while small ice particles with spheric shapes were found to be more ready to bounce off from the test surface, large, nonspheric-shaped ice particles experienced a catastrophic fragmentation process and break up into smaller pieces with noticeable impingement residues remaining on the test surface. The formation of a liquid water film layer on the test surface due to the melting of the impinged ice particles was found to be very beneficial to make more impinged ice particles stay sticking on the test surface, resulting in a rapid growth of the water/ice layer accreted on the heated test surface. A comprehensive theoretical analysis was also performed to examine the unsteady heat transfer characteristics during the dynamic ice accretion process. The theoretic predictions of the collection efficiency of the impinged ice particles on the heated test surface and the temperature variations of the water layer at the initial ice-melting stage were found to agree well with the experimental measurement results.

I. Introduction

IN-FLIGHT icing is widely recognized as one of the most significant hazards to flight safety of airplanes. When an airplane flies through a moisture cloud, airborne supercooled water droplets in the clouds impinge onto airframe surfaces (e.g., aircraft wings, fuselage, and propellers) to cause ice accretion. Ice accretion on aerodynamic surfaces alternates their outer profiles greatly, resulting in a substantial decrease in the aerodynamic lift and a dramatic increase in the drag [1,2]. Without proper icing control/mitigation measures, ice accretion over airframe surfaces directly threaten the flight safety of the airplane [3]. Meanwhile, the impingement and subsequent freezing of airborne supercooled water droplets onto the exposed frontal surfaces of aeroengines, for example, inlet tips, fan spinners, rotor blades, and inlet guide vanes (IGVs), also significantly degrade the engine performance [4–7]. Random ice accretion on the rotating components of aeroengines, such as spinners and fan blades, can also result in an imbalance of the rotating components to cause serious vibrations. Furthermore, ice shedding from the rotating spinner and fan blades may also induce damage to the fan blades and other components behind the fan, even being sucked into the engine core, causing *power-loss* problems, such as stall, surge, and flameout to the aeroengines [8,9].

In addition to the ice accretion caused by airborne, supercooled water droplets, aeroengine icing, especially for jet engines, caused by inhalation of airborne ice particles in high-altitude clouds, has also been found recently to be a rigorous risk for aeroengine operation [10,11]. Ice particles were initially considered not to pose a threat to aviation safety until recent years, as they were believed to simply bounce off from the exposed aeroengine and airframe surfaces. Mason et al. [12] analyzed 46 of a total of 240 engine power loss accidents recorded since 1990 and found that many of the accidents occurred at altitudes above 7000 m where supercooled water droplets barely exist (i.e., the accidents happened outside the icing envelopes given by FAA Appendix C, which were published to guide the design of supercooled water droplet icing protection systems for aircraft). Furthermore, these events commonly take place in the tropics and subtropics area during the spring and summer months [13], which is also completely different from the icing events caused by super-cooled water droplets, which usually take place in cold regions. After a series of comprehensive investigations, it was concluded that the engine power loss events at high altitudes were most likely caused by the inhalation of airborne ice particles into the aeroengine core area. While aeroengine icing has attracted more and more attention in recent years, aeroengine icing due to the inhaled airborne ice particles remains an important unsolved problem [14–20].

In addition to bouncing off from the cold frontal surfaces of aeroengine components (i.e., inlet lip, spinner, and engine fan blades), a certain proportion of airborne ice particles in high-altitude clouds will be inhaled into aeroengine cores, where local air temperature increases gradually and become greater than the water freezing temperature due to the adiabatic compression. By traveling to farther downstream locations of the aeroengine compressors, the inhaled ice particles may be partially or fully melted due to the elevated local temperature. With the impingement of the mixed-phase clouds, a thin layer of liquid water would form on the airflow-passing surfaces of the engine components where the initial surface temperature is above the water freezing temperature. With the increasing amount of ice particles sticking onto the liquid layer, both the liquid water film and warm surfaces will be cooled down below the water freezing temperature to cause ice accretion. The accreted ice layer can block the airflow passing passage inside the engine cores, resulting in an engine stall, surge, and flameout and even structural damage to compressor blades.

Meanwhile, extensive field campaigns have been conducted by meteorologists to characterize the airborne ice particle/crystal properties in high-altitude clouds [21–23]. The measurement data from the field campaigns show that the size of the airborne ice particles/crystals in high-altitude clouds may vary from several micrometers to

*Postdoc Research Associate, Department of Aerospace Engineering; haiyangh@iastate.edu.

†Postdoc Research Associate, Department of Aerospace Engineering.

‡Martin C. Jischke Professor, Department of Aerospace Engineering; huhui@iastate.edu. Associate Fellow AIAA.

a few millimeters in the form of nonspherical shapes, aggregates, and pristine crystals [24]. For example, Yuter et al. [25] conducted a field campaign to characterize the airborne ice particles/crystals in deep updraft clouds at altitudes between 7500 and 11,500 m by using a cloud particle imager probe. They found that the airborne ice particles in convective clouds are complex rime ice particles, which are generated by the collision of original ice particles with supercooled water droplets and aggregation with other ice particles. The rime ice particles were found to be nonspherical in the intermediate and large size range (greater than 100 μm), however, having mostly spherical shape in the smallest size range (less than 100 μm).

While several investigations have been conducted to examine the ice crystal icing process since 2006, most of those studies were performed by the researchers of NASA and the National Research Council of Canada (NRC) [26–29]. Experiments conducted at NRC's Research Altitude Test Facility (RATFac) reveal that, under mixed-phased cloud conditions (i.e., with the local temperature being above the freezing point of water), ice accumulation over the surfaces of compressor blades of aeroengines was directly related to the melt ratio (i.e., the ratio of the liquid to total water content in the airflow) [30]. By applying an axisymmetric model, Currie et al. [31] conducted a numerical study to investigate ice particle melting and evaporation in the RATFac icing tunnel and suggested a severe ice accretion with a melting ratio between 5 to 35%. For the test cases with a melt ratio below this range, ice particles are more likely to bounce off, while limited ice particles at a high melt ratio could also inhibit ice accretion. The characteristics of the ice crystal icing process were also examined recently over the surfaces of a wedge and a NACA0012 airfoil model under the mixed-phase clouds at RATFac and Propulsion System Laboratory [32,33]. Two distinct ice accretion scenarios, i.e., freeze-dominated icing and melt-dominated icing, were evaluated based on a comprehensive surface energy balance analysis. The freeze-dominated icing process is characterized as having strong ice adhesion to the surface, while melt-dominated icing occurring as unmelted ice on a surface accumulates with weakly bonded surface adhesion [32,34]. Apart from the research findings discussed previously, which refer to the conditions defined by surface temperature above the freezing point of water, ice accretion processes at subzero temperatures have demonstrated an enhanced icing severity as the temperature decreases [35]. Baumert et al. [18] conducted an experimental study to examine the ice crystal icing process over the surfaces of a NACA 0012 airfoil model and a cylindrical model at ambient temperatures below the water freezing point. An extended icing severity plateau (i.e., the melting ratio from 0.2 to 0.6) was reported, which is likely due to ice crystal icing turning to supercooled water droplet icing.

Upon the impingement of airborne ice particles in fully glaciated clouds, ice accretion may also occur over the surfaces of heated airframe components, such as on the heated surfaces of pitot tubes and IGVs of aeroengines. In a typical fully glaciated cloud, while local airflow temperatures are well below the water freezing temperature, nearly all the ice particles/crystals are at the glaciated state. In comparison to the extensive studies on mixed-phase cloud icing scenario mentioned previously, only a limited number of investigations can be found in the literature to examine the ice accretion process due to the impingement of ice particles in a glaciated state onto heated surfaces. MacLeod [36] conducted an exploratory study to compare the impingement of a glaciated cloud onto a cold and a heated test plate in NRC's Gas Turbine Laboratory in Ottawa. Rapid ice accretion was observed over the heated test surface at higher ice water content (IWC) values. Ice shedding from the heated test surface due to the aerodynamic shear forces was also observed at the end of the ice accretion cycle. Bucknell et al. [37] examined the heat transfer characteristics of an ice crystal icing process with ice particles impinging onto a heated test plate installed in the Altitude Icing Wind Tunnel at the NRC. Enhancement in the heat transfer was found to increase with both the IWC and mean-volume diameter (MVD) of the ice particles. Hauk et al. [38,39] also conducted an experimental study to investigate the impacting of ice particles onto a heated, unheated, and liquid-covered test surface. A dependency between the ice particle break-up and impact parameters of the

airborne ice particles was established based on the experimental results.

While useful information about the ice crystal icing process has been uncovered from the previous experimental and numerical studies, much more work is still needed in order to improve our understanding of the underlying physics pertinent to aeroengine icing phenomena due to the inhalation of airborne ice particles/crystals. In the present study, a comprehensive experimental campaign is conducted to characterize the dynamic ice accretion process and unsteady heat transfer characteristics upon the impingement of airborne, microsized ice particles onto a heated test plate. The experimental study was conducted by leveraging a newly developed ice crystal icing test facility located at Iowa State University to generate microsized, glaciated ice particles and inject them into a small wind tunnel hosted inside a walk-in freezer with the ambient temperature maintained at -10.0°C. While microsized ice particles carried by frozen-cold airflow were forced to impinge onto the front surface of a heated test plate at the impacting speed of 40 m/s, an electrical film heater was embedded on the back side of the test plate to adjust the surface temperature of the test plate for different test conditions. During the experiments, in addition to using high-resolution imaging systems to record the dynamic ice accretion process over the heated test surface from different perspectives, a high-speed imaging system along with a 60X microscopic objective was also used to characterize the impingement morphology of individual ice particles to gain further insight into the underlying physics. Furthermore, a high-speed IR thermal imaging system along with high-precision thermocouples at the points of interest was also used to map the corresponding surface temperature distributions on the test plate to quantify the unsteady heat transfer characteristics during the dynamic ice accretion process. The objective of the present study is to improve our understanding of the ice crystal icing process pertinent to aeroengine icing phenomena, which is essential for the development of effective and robust antiicing/deicing strategies to ensure safe and efficient aeroengine operation in high-altitude clouds.

II.   Experimental Setup

A.   Brief Introduction of Ice Crystal Icing Test Rig Used for Present Study

The experimental study was conducted by leveraging a specially designed ice crystal icing test facility available at the Aerospace Engineering Department of Iowa State University. The entire test facility is installed in a large frozen chamber (i.e., with its dimension of 6 ft in width by10 ft in length by 6 ft in height), in which the ambient temperature can be well controlled down to -20°C with a variation within $\pm 10^\circ$C. As shown schematically in Fig. 1, a high-thrust electric duct fan (JP 90 mm 8S EDF) powered by a dc power supply system (i.e., VOLTEQ HY3050FX^{TM}) is installed at the inlet of a cylindrical wind tunnel to drive frozen-cold air flowing into the wind tunnel. The velocity of the airflow exhausted from the circular nozzle ($D_{nozzle} = 76$ mm) of the wind tunnel is adjustable from $V_\infty = 0$ to 100 m/s via an electronic speed controller ($V_\infty = 40$ m/s for the present study). Microsized ice particles are injected into the wind tunnel via a T-shaped connector to become airborne ice particles and then exhaust from the wind tunnel exit. A high-pressure-driven sieving system is used to control the total amount of ice particles injected into the airflow to adjust the IWC level in the airflow. It should be noted that the IWC level in the airflow was set at IWC ≈ 5.0 g/m^3 for all the test cases of the present study, which was calibrated by weighing the ice particles exhausted from the wind-tunnel exit before carrying out the ice crystal icing experiments. After being exhausted from the tunnel exit, the ice particles carried by the frozen-cold airflow impinged onto a heated test plate mounted in the middle of a transparent impingement test chamber.

The glaciated ice particles/crystals used for the present study were generated in a specially designed chest freezer. As shown schematically in Fig. 1a, a chest freezer filled with a layer of dry ice (i.e., the solid form of carbon dioxide of approximately 100 mm in layer thickness) at the bottom of the chest freezer was used to generate a low-temperature environment (i.e., temperature below -30°C).
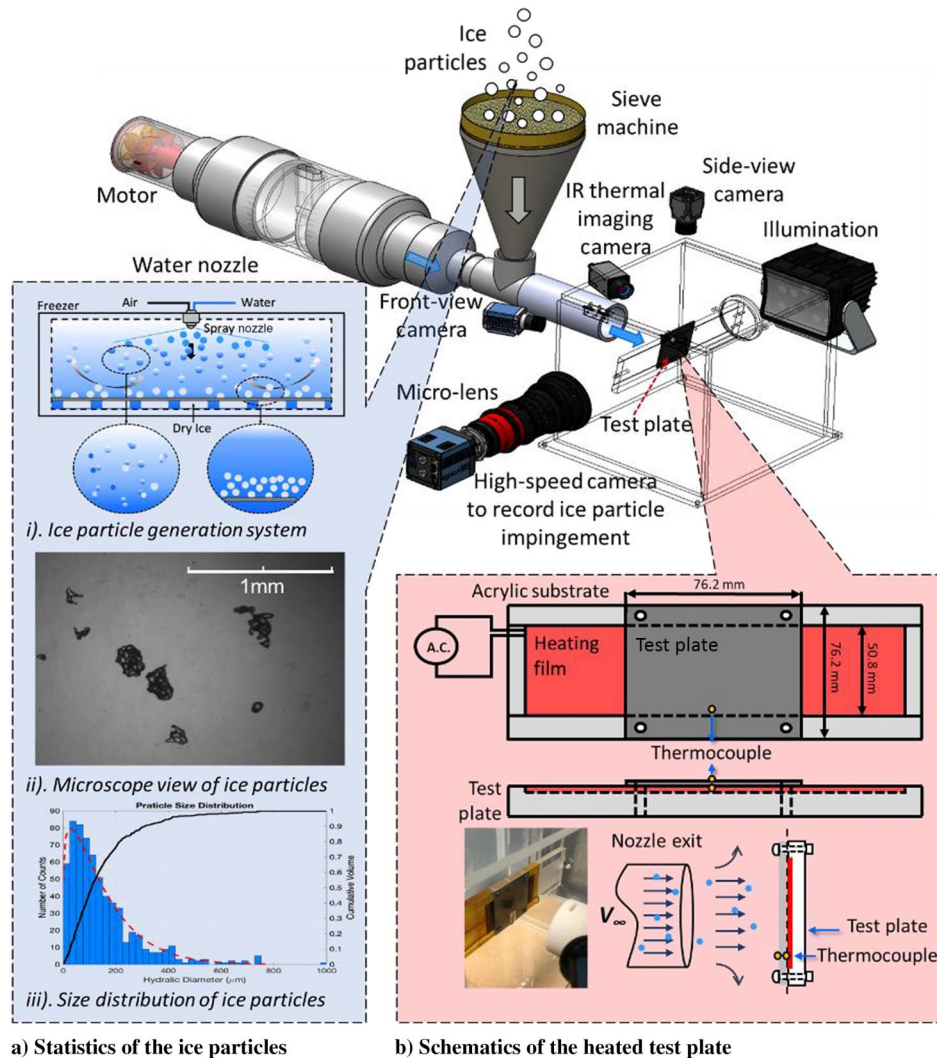
Fig. 1 Experimental setup used for the present study.

A spray nozzle/atomizer (i.e., IKEUCHI BIMV-8002) was installed on the top cover to inject microsized water droplets into the chest freezer. While deionized water is supplied to the spray nozzle for water droplet generation, the size of the water droplets exhausted from the spray nozzle/atomizer can be adjusted by manipulating the pressure levels of the air and water lines supplied to the spray nozzle/ atomizer. With the parameter settings used in the present study, the water droplets exhausted from the spray nozzle/atomizer were found to be in the range from 10 to 100 μm in size, with the MVD value being about 20 μm, as measured by using a LaVision's ParticleMaster™ system.

After being exhausted from the spray nozzle/atomizer, the microsized water droplets will be frozen into ice particles rapidly during the falling process toward the bottom of the chest freezer. A recirculating airflow was generated inside the deep chest freezer to enable the falling ice particles to collide and aggregate with other water droplets or ice particles to form large, nonspherical-shaped, large ice particles. Figure 1a also gives an example of the acquired image to reveal the morphology of the ice particles collected at the bottom of the chest freezer, which was acquired by placing the ice particles on the glass slide of a 20X magnification microscope. A comprehensive image-processing procedure, including Gaussian filtering for noise reduction and background removal, binary treatment for edge enhancement, and a Canny method for edge identification, was used to extract quantitative morphology information from the acquired images of the ice particles. Based on the acquired images of approximately 2000 ice particles, the statistics about the size distribution of the ice particles generated inside the chest freezer were determined in terms of the

hydraulic diameter. The MVD values of the ice particles used for the present study were found be approximately 100 μm.

B. Heated Test Plate Used for Present Study

The test plate used in the present study is made of aluminum with a high thermal conductivity (i.e., $K = 236$ W/m · K [40]). It has a dimension of 76.2 mm in height by 76.2 mm in width and 10.0 mm in thickness. As shown schematically in Fig. 1b, the test plate was mounted on an acrylic support beam in the middle of a transparent impingement test chamber. A thin electric film heater (i.e., DuPont™ Kapton® RS with a film thickness of 500 μm) was sandwiched between the acrylic support beam and the back of the test plate. The film heater was connected to an ac transformer to manipulate the power input levels, thereby changing the temperature on the front surface of the test plate for different test conditions. While the impinging angle of the ice particle-laden airflow onto the test plate can be adjusted (i.e., ranging from 0 to 90 deg), the test plate was oriented vertically for all the test cases of the present study. As a result, the airborne ice particles impinged normally onto the front surface of the heated test plate with the impinging angle being 90 deg.

C. Measurement Systems Used in Present Study

During the experiments, a high-resolution digital camera (i.e., Nikon D 50 camera with 2048 × 2048 pixels at the frame rate of 24 Hz) along with a Nikon 60 mm lens (i.e., Nikkor 2.8D) was mounted at about 300 mm above the test plate to record the dynamic ice accretion process on the heated test surface. Meanwhile, another digital camera (i.e.,

ImagingSource, DMK 23U618 with 640×480 pixels in spatial resolution at the frame rate of 120 Hz) was used to acquire the *side-view* images of the ice accreting test plate to quantify the thickness growth of the water/ice layer accreted on the test plate. While the measurement window size of the side-view camera was set to be about 50×40 mm in the middle of the test plate, the corresponding spatial resolution of the acquired images was estimated to be approximately 10.0 pixels/mm.

To gain further insight into the underlying physics pertinent to the dynamic impinging process of airborne ice particles, a high-speed imaging system (i.e., Photron, FASTCAM Mini WX100 camera with the frame rate up to 10 KHz with a spatial resolution of 1000×1000 pixels) along with a 60X microscopic lens was also used to record the dynamic impinging process of the individual ice particles onto the surface. The high-speed imaging system was positioned normal to the front surface of the test plate with the measurement window size being 3.0 mm $\times$ 3.0 mm. The corresponding spatial resolution of the acquired images was estimated to be approximately 300 pixels/mm.

In addition to recording the dynamic ice accretion process with the digital cameras from different perspectives, a high-speed IR thermal imaging system (FLIR-A615 with 640×480 pixels in spatial resolution) was also used in the present study to map the temperature distributions over the surface of the test plate under different test conditions. The IR thermal imaging camera was mounted 300 mm away from the test plate to acquire the IR thermal images via an IR transmission window (FLIR-IRW-4C) installed on the top wall of the transparent test chamber. The IR thermal imaging system incorporates a new interface standard of GigE Vision, which allows for fast image transfer to achieve 16 bit thermal imaging outputs at a frame rate up to 200 Hz. A calibration procedure similar to that described by Liu and Hu [16] was performed to verify/validate the IR thermal imaging measurement results at several prescribed low temperatures (i.e., down to -20.0°C) before starting the icing experiments. Within the measurement range of the present study, the uncertainty of the IR thermal imaging measurement was estimated to be $\pm 0.25^\circ$C.

Several K-type thermocouples were also flush mounted on both the front and back surfaces of the test plate to monitor the temperature variations of the test plate during the icing experiments. The thermocouple measurements at the points of interest were correlated with the IR imaging results to quantify the unsteady heat transfer characteristics over the surface of the heated test plate under different test conditions. An integrated temperature and relative humidity sensing system was also employed to monitor the ambient conditions (i.e., temperature and humidity) inside the test chamber. The measurement uncertainty of the thermocouples was estimated to be $\pm 0.20^\circ$C.

D. Experimental Procedure and Test Conditions of Present Study

Before starting the ice accretion experiment, while the walk-in frozen chamber was cooled down to the preselected ambient temperature (i.e., $T_{ambient} = -10^\circ$C for the present study), the high-thrust electric duct fan of the wind tunnel was switched on for at least 10 min to enable the entire system to reach a thermal equilibrium state. By manipulating the power input supplied to the electric film heater attached to the backside of the test plate, the surface temperature of the aluminum test plate was maintained at the prescribed values for the ice crystal icing experiments under different test conditions. The film heater was operated in a constant power input mode to ensure a constant thermal flux supplied to the test plate during the icing experiments. Two sets of K-type thermocouples were flush mounted on the surface of the heated test plate to monitor the variations of the surface temperature during the ice accretion experiments.

After the entire system reached an equilibrium state at the prescribed temperatures, the sieve machine was turned to inject microsized ice particles into the wind tunnel at the preselected feeding rate. As a result, the microsized ice particles carried by the frozen-cold airflow would impinge normally onto the surface of the heated test plate inside the impingement chamber. During the experiments, while the impinging airflow velocity at the exit nozzle of the wind tunnel was set at $V_\infty = 40$ m/s, the IWC level in the airflow was

Table 1 The primary parameters of the test cases of the present study

Test case	Initial surface temperature of the test plate T_{plate}, C	Temperature of the incoming airflow T_∞, °C	IWC level in the incoming airflow, g/m^3	Impinging speed of the ice particle laden airflow V_∞, m/s
1	-8.5	-10.0	5.0	40.0
2	$+10.0$	-10.0	5.0	40.0
3	$+20.0$	-10.0	5.0	40.0
4	$+30.0$	-10.0	5.0	40.0

fixed at 5.0 g/m^3 (i.e., IWC = 5 g/m^3). In the present study, a comparative study was conducted with the initial surface temperature of the test plate being set at four different levels, including an unheated test case (i.e., without turning on the film heater at the backside the test plate) as the comparison baseline and three heated test cases with the film heater being switched on but at different supplied power levels. The primary parameters of the test cases invested in the present study are summarized in Table 1.

It should be noted that the experiments under each test condition were repeated at least three times to check the repeatability of the experimental results. While almost the same experimental results were obtained under the same test conditions, only the typical measurement results are presented here for conciseness.

It is also worth noting that the thermocouple mounted on the front surface of the test plate measured the stagnation temperature (i.e., total temperature) of the ice particle laden airflow. With the ambient temperature was set at $T_{amb} = -10^\circ$C, the total temperature on the test plate should be about -9.2°C theoretically, with the impinging speed of the frozen-cold airflow being at $V_\infty = 40$ m/s. However, in reality, the measured total temperature on the test plate for the unheated test case (i.e., without turning on the electric film heater) was found to be -8.5°C (i.e., $T_{plate} = -8.5^\circ$C), which is slightly higher than the theoretical prediction value of -9.2°C. It is believed to be due to the effects of the friction heating associated with the transportation of microsized ice particles laden in the impinging airflow.

III. Measurement Results and Discussions

A. Characteristics of Ice Accretion Process over Test Surface Under Different Test Conditions

Figure 2 gives typical snapshot images acquired by using the front-view camera to visualize the dynamic ice accretion process over the test plate upon the impingement of airborne ice particles under different test conditions. As shown clearly in Fig. 2a, for the test case without turning on the electrical film heater (i.e., the test plate being frozen cold with $T_{plate} = -8.5^\circ$C), almost all the impinging ice particles were found to bounce off rapidly from the frozen-cold surface of the test plate. As a result, while no obvious ice accretion was observed on the test surface, only very small fractions of the impinged ice particles were found to remain on the test surface as the impingement residues from time to time (i.e., the isolated bright spots shown in Fig. 2a). The impingement residues were found to be washed away eventually by the aerodynamic shear forces exerted by the ice particle-laden airflow.

When the test plate was heated up with its surface temperature becoming greater than the water freezing temperature (e.g., the test case with $T_{plate} = +10.0^\circ$C shown in Fig. 2b), much more complicated interactions among the multiphase flow system (i.e., the impinging airflow, airborne ice particles, and melting ice/water flows on the heated test surface) were observed to cause an obvious ice accretion on the surface of the heated test plate. The phase-changing process of the impinged ice particles (i.e., the dynamic ice accretion process) over the heated test surface was observed to take place in three distinct stages, which include 1) a melting stage of the impinged ice particles at the beginning of the experiment, followed by 2) an ice/water mixture formation stage, and then 3) a liquid water refreezing stage (i.e.,

a) The unheated test case (i.e., with $T_{wall,}$ = -8.5°C

b) The heated test case with T_p = +10.0°C

c) The heated test case with T_p = +20.0°C

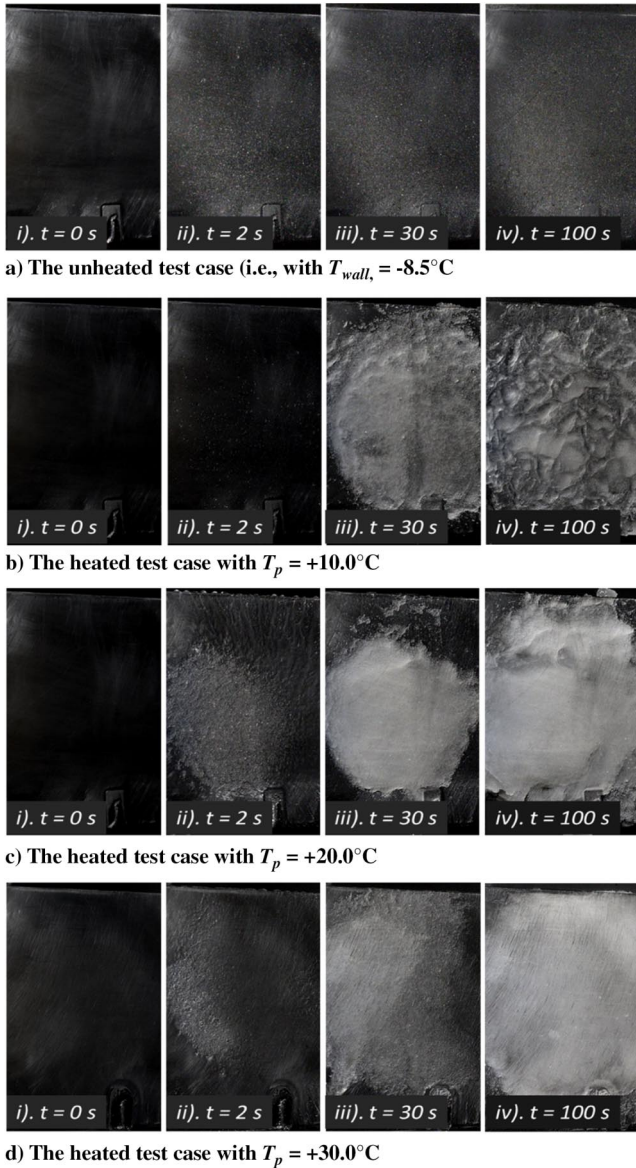**d) The heated test case with T_p = +30.0°C**

Fig. 2   Typical snapshots of the acquired images to reveal the dynamic ice accretion processes over the test surface upon the impingement of airborne ice particles under different test conditions.

solidification stage), causing the formation of a solid ice layer accreted on the heated test surface eventually. As revealed from the snapshot images acquired at $t = 2.0$ s given in Fig. 2, a portion of the impinged ice particles were found to be melted into the liquid water upon impinging onto the heated test surface. While the surface water from the melted ice particles was observed to coalesce rapidly to form a thin water film over the test surface, the surface temperature of the test plate was found to decrease rapidly due to the absorption of the latent heat of fusion associated with the liquefaction process (i.e., the temperature measurement results will be presented later). With the existence of the liquid water layer on the test surface, impinged ice particles were found to be more readily to adhere to the wetted test surface, instead of bouncing off from the test surface. As a result, a *slushy layer*, which consists of a mixture of liquid water and solid ice, was found to accrete on the heated test surface (i.e., transition to ice/water mixture stage), as revealed clearly in the images acquired at $t = 30$ s given in Fig. 2.

With the continuous impingement of the ice particles carried by the frozen-cold temperature at $T_\infty = -10°$C, the temperature of the water/ice mixture layer accreted over the test surface was found to decrease gradually due to the intensive convective heat transfer to the frozen-cold airflow, causing the water/ice mixture layer to have a subzero temperature eventually. As a result, the liquid water in the

ice/water mixture would be refrozen into ice, causing the formation of a solid ice layer on the heated test plate, as revealed clearly from the image acquired at $t = 100$ s shown in Fig. 2b. The slushy layer (i.e., ice/water mixture layer) accreted on the heated test surface was found to turn into a transparent glazy ice layer eventually (i.e., transition to the water refreezing stage). After the liquid water was refrozen into ice completely, while the test plate was covered by a layer of solid ice, the continuous impingement of airborne ice particles was found to cause erosion to the surface of the solid ice layer accreted on the heated test surface.

As revealed clearly from the acquired images given in Fig. 2c, for the test case with a higher surface temperature (i.e., $T_{\text{plate}} = +20°$C), more obvious melting of the impinged ice particles was observed on the heated test surface. It indicates that, corresponding to the higher thermal flux supplied to the test plate, more impacted ice particles melt into liquid water right after striking the *warmer* test surface. In addition to having a thicker liquid water film accumulated over the test surface, the formation of the slushy flow (i.e., ice/water mixture layer) also took place much earlier (i.e., a slushy flow was observed in the image acquired at $t = 2$ s as shown in Fig. 2c, in comparison to that at $t = 30$ s for the test cases with $T_{\text{plate}} = +10°$C). The water refreezing process was also found to complete much faster with the formation of a glazy ice layer on the test surface within 80 s of the icing experiment for this test case.

Figure 2d illustrates the ice accretion process for the test case with the surface temperature of the test plate being increased to $T_{\text{plate}} = +30°$C. While more impinged ice particles were found to melt into liquid water to form a much thicker water film onto the *hot* test surface, the ice/water mixture layer formed over the test surface was found to become more readily to form, due to the existence of a larger portion of liquid water for this test case. Driven by the aerodynamic shear forces exerted by the impinging airflow over the test plate, the ice/water mixture was found to flow and then shed from the test surface before being refrozen into solid ice. As a result, a continuous slushy flow of the ice/water mixture was found to move over the test surface during the entire icing experiment. Unlike those cases with lower surface temperatures, no solid ice layer was found to accrete over the test surface for this test case.

In the present study, a high-speed digital camera was also used to acquire side-view images of the water/ice layer accreted over the test surface under different test conditions. By using a comprehensive image processing procedure similar as that described by Waldman and Hu [41] and Liu et al. [42], the quantitative information, such as the thickness changes of the water/ice layer accreted on the test plate, was extracted from the time sequences of the acquired side-view images. Figure 3 shows the measurement results to reveal the time
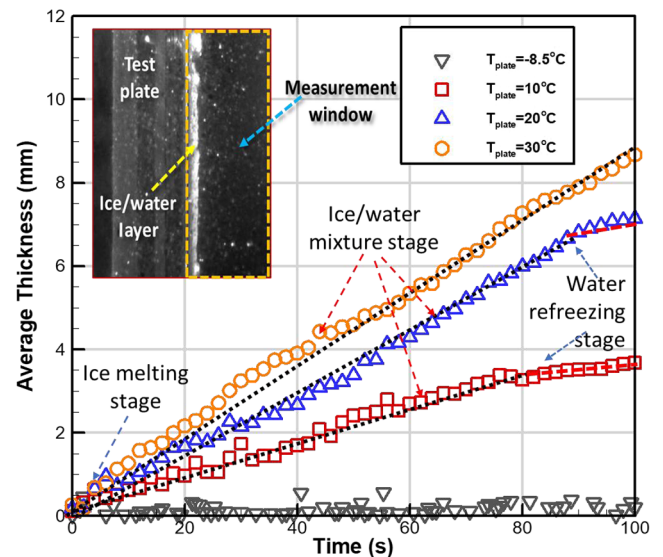

Fig. 3   Time evolution of the averaged thickness of the water/ice layers accreted on the test surface.

evolution of the averaged thickness of the water/ice layer (accreted on the heated test surface, i.e., the averaged thickness of the water/ice layer within the measurement window given in Fig. 3) under different test conditions. It can be seen clearly that, because almost all the impacted ice particles were bouncing off from the frozen-cold test surface (i.e., the test case with $T_{plate} = -8.5°C$), the thickness of the ice/water layer on the test surface was found to be almost zero for the unheated test case, as expected. However, after turning on the electrical film heater to heat up the test plate with the test surface temperature becoming higher than the water freezing temperature, the thickness of the water/ice layer accreted on the test surface was found to increase almost linearly as time progressed, in general. The growth rate of the water/ice layer accreted on the heated test surface was found to vary greatly, depending on the surface temperature of the test plate. The water/ice layer accreted on the test surface was found to increase monotonically with the increasing surface temperature of the test plate. It indicates that, correlating well with a greater amount of the thermal flux supplied by the electrical film heater to the test plate, more impinged ice particles would be melting into liquid water, resulting in the faster growth of the ice/water layer accreted on the test surface with higher test surface temperature.

It can also be seen that, once the liquid water in the water/ice mixture layer was refrozen into solid ice at the later stage of the ice accretion experiments (i.e., after the transition into the water refreezing stage), the growth rate of the ice layer accreted on the test surface was found to slow down substantially, in comparison to the ice thickness increase rate at the initial ice-melting stage and ice/water mixture formation stages. This is believed to be caused by the more likely bouncing off of the impinging ice particles from the surface of the solid ice layer than those from the wetted water/ice mixture layer for the test cases of $T_{plate} = +10°C$ and $T_{plate} = +20°C$.

Because the impinging speed V_∞ and IWC in the incoming airflow were fixed at the same values during the experiments, the total mass of the water/ice layer accreted on the test plate can be estimated by using the equation

$$m = \beta \cdot IWC \cdot V_\infty \cdot t \cdot A \tag{1}$$

where β is the collection efficiency of the impinging ice particle on the test surface (i.e., the ratio of the mass of the impinged ice particles remaining on the test surface to the total mass of the ice particles impinging onto the test surface), t is the ice accumulation time, and A is the impingement area. Therefore, the growth rate of the ice layer thickness on the test surface per unit area can be calculated as

$$\dot{L}_{thickness} = \frac{\dot{m}}{\rho A} = \frac{1}{\rho A} \cdot \frac{d(\beta \cdot IWC \cdot V_\infty \cdot t \cdot A)}{dt} = \frac{\beta \cdot IWC \cdot V_\infty}{\rho} \tag{2}$$

It can be seen that, according to Eq. (1), the thickness of the ice layer accreted on the test surface has a linear relationship with the collection efficiency of the impinging ice particles on the test surface. Based on Eq. (2), the collection efficiency of the impinging ice particles on the test surface can be estimated from the measured growth rate of the ice layer accreted on the test plate.

As shown clearly in Fig. 3, while the ice/water layer accreted on the test plate was found to increase almost linearly with the ice accretion time at the initial ice-melting stage and the ice/water mixture formation stage, the growth rate of the ice/water layer was found to be 0.039 mm/s for the test case with $T_{plate} = 10°C$. Therefore, based on Eq. (2), the collection efficiency of the impinging ice particles on the test surface was estimated to be 24% for the test case with $T_{plate} = 10°C$. With the same procedure, while the collection efficiency of the impinging ice particles was found to become approximately 37% for the test case with $T_{plate} = +20°C$, the corresponding value was found to increase to approximately 42% when the surface temperature of the test plate was increased to $T_{plate} = +30°C$. It implies that the collection efficiency of the impinging ice particles increases monotonically with the increasing surface temperature of the test plate. This can be explained by the fact that, for the test case with a higher surface temperature, a larger amount of ice particles

melted into liquid water upon impinging onto the heated test surface at the initial ice-melting stage of the ice accretion process, causing a thicker layer of liquid water film accumulated on the test surface. Furthermore, a larger portion of the liquid water within the ice water layer during the subsequent ice/water mixture formation stage would keep the test surface wetted to capture more impinged ice particles sticking to the test surface. However, after the water/ice mixture layer accreted over the test plate was refrozen completely into solid ice (i.e., after the transition to water refreezing stage), the impinged ice particles was more likely to be bouncing off from the surface of the solid ice layer accreted over the test plate, and only small fragments of the impinged ice particles were able to stick to the surface of the solid ice layer as the impingement residues, resulting in a much slower growth rate of the ice layer accreted on the test surface. As illustrated clearly in Fig. 3, while the growth rate of the ice/water layer accreted on the test plate was found to be reduced to 0.021 mm/s after the transition to the water refreezing stage for both the test cases of $T_p = 10°C$ and $T_p = 20°C$, the corresponding collection efficiency of the impinged ice particles was estimated to become only 13%.

B. Microscopic Imaging Results to Characterize Dynamic Impinging Process of Ice Particles

In the present study, a high-speed, high-resolution microscopic imaging system (i.e., with a 60X microscopic objective at the image acquisition frame rate up to 10 KHz) was also used to examine the impingement morphology of airborne ice particles under different test conditions. Figure 4 gives some typical snapshots images to reveal the general features of the dynamic impinging process of airborne ice particles onto the test surface for two selected scenarios, i.e., airborne ice particles were impinging onto 1) the frozen-cold test plate with $T_p = -8.5°C$ and 2) heated test surface with $T_p = +30.0°C$. During the experiment, while the relevant airflow parameters were still set to be $V_\infty = 40$ m/s and $T_\infty = -10°C$, the IWC level in the incoming airflow was reduced to IWC = 1.0 g/m³ to minimize the interferences among the airborne ice particles.

As shown clearly in Fig. 4a, upon the impingement of ice particles onto the frozen-cold test surface, while most of the impinged ice particles were found to bounce off from the rigid test surface, some minor fragments of the impinged ice particles were observed to remain on the test surface as the impingement residues due to the complicated interactions among the impinging ice particles, local airflow, and the surface roughness of the test plate. With the continuous impingement of the airborne ice particles, the total amount of the impingement residues sticking onto the test surface was found to

a) Ice particle impinging onto frozen-cold test surface   b) Ice particle impinging onto heated test surface
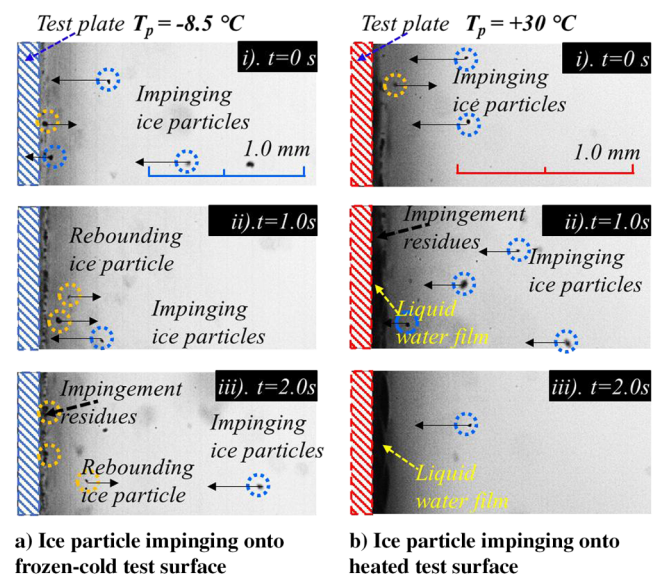
Fig. 4 Acquired snapshot images to reveal the impinging characteristics of individual ice particles onto the test surface under different test conditions.

remain almost the same, as shown clearly in Fig. 2a. It suggested that, while some fragments of the newly impinged ice particles may stick on the test surface as the impingement residues, the existing impingement residues could be washed away from the test surface due to the aerodynamic shear forces exerted by the incoming airflow over the test surface.

The acquired images given in Fig. 4b reveal clearly that, with the surface temperature of the test plate being greater than the water freezing temperature, while some impinged ice particles were still found to bounce off from the test plate at the beginning of the impinging experiment, most of the impinged ice particles were found to melt into liquid water, resulting in the formation of a liquid water film accreted over the heated test surface. Because of the existence of the liquid water layer on the heated test plate, much fewer impinged ice particles were found to bounce off from the test surface. With continuous impingement of the airborne ice particles onto the heated surface, more impinged ice particles will be melting into liquid water, causing the rapid growth of the liquid water layer accreted on the heated test surface, as shown clearly in Fig. 4b. As time progresses, more and more impinged ice particles will be captured by the water film, resulting in the formation of a slurry flow (i.e., water/ice mixture layer) on the test surface.

Figure 5 gives the time sequences of the acquired images for three selected ice particles as they are impinging onto the rigid, frozen-cold test surface, which can reveal further details about the impinging characteristics of the airborne ice particles. As shown clearly in Fig. 5a, upon impinging onto the rigid test surface, tiny ice particles (i.e., with the MVD being smaller than 100 μm), which comprise about 50% of the total impinged ice mass for the test cases of the present study, were found to bounce directly off the test surface without any observable fragmentations or impingement residues sticking to the test surface. The bouncing-off ice particles were found to have much smaller flying speeds in comparison to the impinging ice particles, confirming the inelastic collision nature of the ice particle impinging process.

After midsized ice particles (i.e., the MVD value between 100 and 200 μm) impinged onto the test surface, an obvious fragmentation process was observed, as shown clearly in Fig. 5b, resulting in the rapidly breaking up of the impinged particles into multiple smaller pieces. It should be noted that, while the total mass of the ice particles with their size under 200 μm comprises about 70% of the total impingement ice mass for the test cases of the present study, the ice particles (i.e., the small and midsized ice particles) were found to be almost spherical in shape. After impinging onto the rigid test surface, almost all the impinged ice particles were found to bounce off from

the test surface without any noticeable impingement residues remaining on the test surface, as revealed clearly in Figs. 5a and 5b.

As revealed from the field measurements of Yuter et al. [25] and visualized clearly in Fig. 1a, large ice particles (i.e., ice particles with their MVD greater than 200 μm) were found to have much more complicated nonspherical shapes due to the aggregation of multiple small pristine crystals. Catastrophic fragmentations were observed upon the impingement of large-sized ice particles onto the rigid test surface, as revealed from the acquired images given in Fig. 5c. Large ice particles were found to be breaking up into many tiny ice particles. While a majority of the splashed fragments were found to be bouncing off from the test surface, a small fraction of the impinged ice particles was found to be sticking onto the test surface as the impingement residues. With continuous impingement of ice particles with different sizes, the impingement residues on the test plate were found to be blown away by other impinging ice particles and/or airflow. In summary, noticeable residues were found to remain on the test surface after the impingement of large ice particles (i.e., MVD > 200 μm), which counts for 30% of the total impinged ice mass for the test cases of the present study.

C. Characteristics of Temperature Variations on Test Surface During Ice Accretion Process

In the present study, while a high-speed IR thermal imaging system was used to achieve time-resolved temperature measurements on the upper surface of the water/ice mixture layer accreted on the test surface, a thermocouple was used to measure the corresponding surface temperature of the test plate. Figure 6 gives the measured temperature data on both the outer surface of the water/ice layer (i.e., T_{IR}, the IR thermal imaging results) and the surface of the test plate (i.e., T_p, measured by using the thermocouple). It should be noted that, because the IR thermal imaging results were found to be rather uniform within the measurement window, as shown in Fig. 6, only the averaged values were presented in the plots to compare with the thermocouple measurement results. The measured ambient temperature (i.e., T_{∞}) during the dynamic ice accretion process was also plotted in the figures as the reference baseline.

As aforementioned, the dynamic ice accretion process on the heated test surface due to the impingement of airborne ice particles can be divided into three distant stages (i.e., an ice-melting stage at the beginning, followed by a water/ice mixture formation stage, and then a water refreezing stage). The unique features of the three distinct stages are revealed clearly from the temperature measurement results given in Fig. 6. It can be seen clearly that the surface

a) Small-sized ice particle with MVD ≈ 60 μm b) Midsized ice particle with MVD ≈ 60 μm c) Large-sized ice particle with MVD ≈ 600 μm
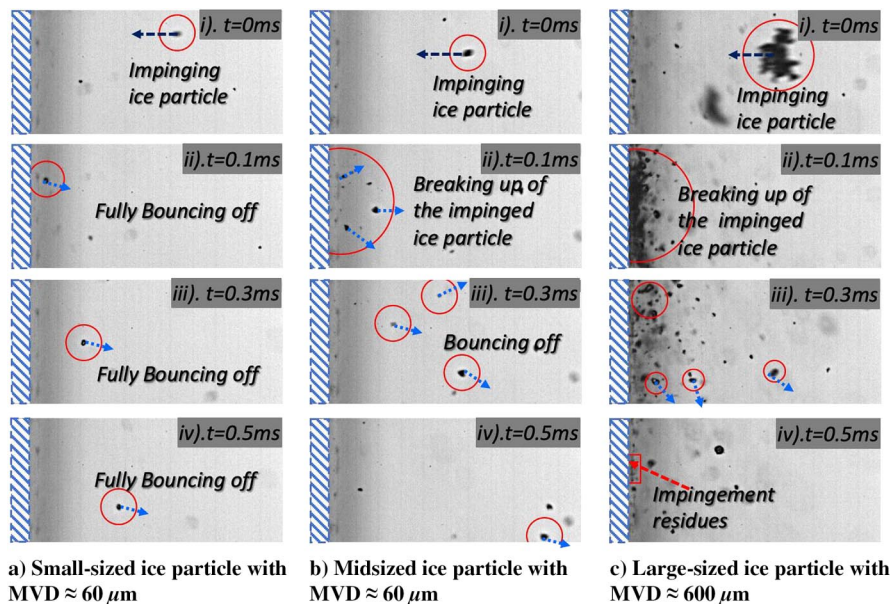
Fig. 5 Time sequences of the acquired snapshot images to reveal the dynamic impinging processes of airborne ice particles onto the frozen-cold test surface.
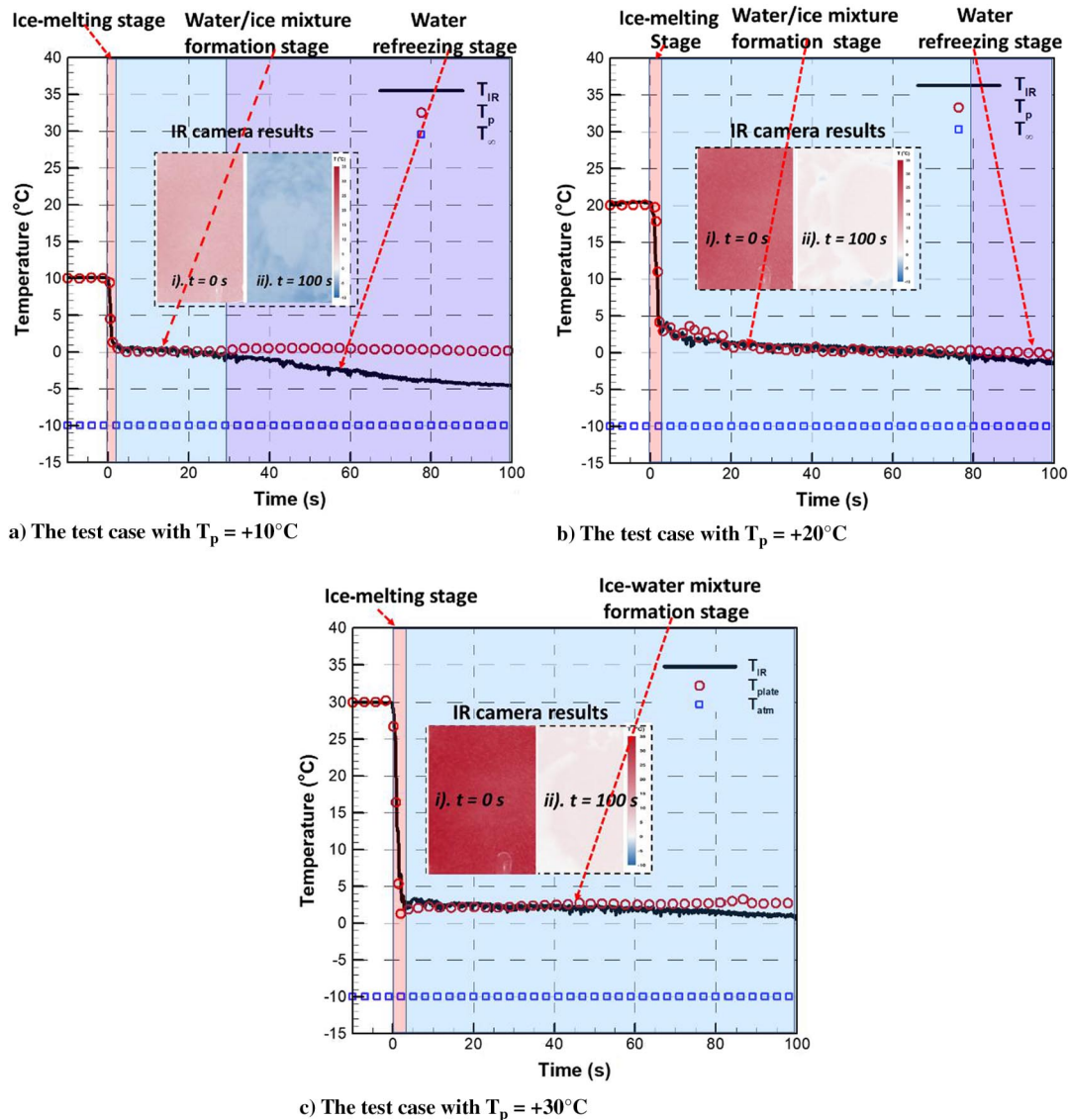
Fig. 6   Time evolution of the measured surface temperatures on the outer surface of the water/ice layer and the test plate under different test conditions.

temperature of the test plate was found to experience a rapid decrease upon the impingement of the airborne ice particles onto the heated test surface for the test case with $T_p = 10^{\circ}C$, as shown clearly in Fig. 6a. The rapid decrease of the measured temperatures is believed to be caused by the absorption of the latent heat of fusion associated with the liquification of the impinged ice particles at the initial stage of the experiment (i.e., the ice-melting stage within the first 2 s of the experiment). While a thin layer of liquid water film was found to accumulate on the heated test surface due to the melting of the impinged ice particles, the temperature on the outer surface of the accumulated water film (i.e., measured by using the IR thermal imaging system) was found to be slightly higher than the water freezing temperature (i.e., $\geq 0^{\circ}C$), which is almost the same as the surface temperature of the test plate (i.e., measured by using the thermocouple) at the initial ice-melting stage.

As time progresses, more and more airborne ice particles impinged onto the test surface. However, because of the limited thermal flux supplied to the test plate, only a portion of impinged ice particles could be able to melt into liquid water, while the rest of the impinged ice particles would be captured by the water film and stay in solid ice without undergoing the phase change process. As a result, a layer of water/ice mixture is formed on the test surface, i.e., the formation of a water/ice mixture layer with a rough surface and milk-white appearance, as shown in Fig. 2b. I can also be seen that the temperatures of both the thin water film and the test plate were found to stay almost

unchanged near the water freezing temperature (i.e., $T_{\text{surface}} \approx 0.0^{\circ}C$) for a while (i.e., up to $t = 20$ s) during the water/ice mixture formation stage.

With continuous impingement of the ice particles carried by the frozen-cold airflow at $T_{\infty} = -10^{\circ}C$, the intensive convective heat transfer to the frozen-cold airflow was found to cause a gradual decrease of the temperature on the outer surface the water/ice mixture layer. However, the temperature on the test surface (i.e., the inner surface of the ice/water mixture layer) was still found to stay almost unchanged at $T_p \approx 0.0^{\circ}C$. This indicates that the water/ice mixture layer accreted over the heated test surface acted as a thermal insulation layer to suppress the dissipation of the thermal flux supplied by the film heater from the test plate to the frozen-cold airflow.

As the temperature on the outer surface of the water/ice mixture layer became lower than the water freezing temperature, the liquid water in the water/ice mixture layer was refrozen into solid ice (i.e., starting the water refreezing stage at $t > 30$ s, as shown quantitatively in Fig. 6a). During the water refreezing stage, the rough water/ice mixture layer on the test surface was found to evolve into a transparent, glazy ice layer with rather smooth surface, as shown in Fig. 2. After starting the water refreezing process, the temperature on the outer surface of the accreted ice layer was found to decrease monotonically as the time progresses. It should also be noted that the temperature on the surface of the test plate (i.e., the inner surface of the ice layer accreted on the test surface) was found to stay around the

water freezing temperature of $T_{\text{water−freezing}} = 0.0°C$ during the entire water refreezing process.

As shown in Fig. 6b, with a higher thermal flux supplied to the test plate (i.e., the test case with $T_p = +20°C$), while a rapid decrease of the surface temperature on the test plate at the initial ice-melting stage (i.e., within the first 2 s of the experiment) was found to be very similar as that of the test case with $T_p = +10°C$, the water/ice mixture formation stage was found to become much longer, due to the existence of a larger amount of liquid water in the water/ice mixture layer accreted on the heated test surface. More specifically, the IR thermal imaging results reveal that the outer surface of the water/ice mixture layer accreted on the heated test surface stayed above the water freezing point (of $T_{\text{surface}} > 0.0°C$) until $t \approx 80$ s, indicating that the water refreezing process stage did not start until $t \approx 80$ s as shown quantitatively in Fig. 6b. In comparison, the water refreezing process stage was found to start much earlier i.e., $t \approx 30$ s for the test case with $T_p = +10°C$.

With the surface temperature of the test plate being further increased to $T_p = +30°C$, more ice particles melted into liquid water upon impingement, resulting in a thicker water film layer accumulated on the test surface. As shown quantitatively in Fig. 6c, while the surface temperature of the test plate was still found to decrease rapidly at the initial ice-melting stage (i.e., within the first 2 s of the experiment), the temperatures on both the outer surface of the water film layer and the test surface were found to stay at slightly above the water freezing temperature ($T_{\text{surface}} > 0.0°C$) during the entire duration of the experiment of the present study (i.e., the entire duration of 100 s). It suggests that the water film layer accumulated over the heated test surface always stay in the liquid phase, despite the continuous impingement of the ice particles carried by the frozen-cold airflow. As a result, no water refreezing process was observed due to the much higher thermal flux supplied to the test plate for this test case.

D. Theoretical Analysis of Unsteady Heat Transfer Characteristics During Ice Accretion Process

A comprehensive theoretic analysis was also conducted in the present study to examine the unsteady heat transfer characteristics during the different stages of the ice accretion process. As shown schematically in Fig. 7, energy conservation law can be applied to an arbitrarily chosen control volume on the surface of the test plate during the ice accretion process.

As aforementioned, upon the impingement of airborne ice particles onto the heated test surface, a portion of the impinged ice particles experience a rapid phase change process (i.e., the transition from the solid ice state to the liquid water state) during the initial ice-melting stage. Because a substantial amount of heat would be absorbed associated with the liquefaction process, the temperatures of both the test plate and the water film accumulated on the test surface experienced a rapid decrease due to the absorption of the latent heat of fusion due to the melting of impacted ice particles.

Almost no temperature differences were observed between the outer surface of the accumulated water film (i.e., measured by using the IR thermal imaging system) and the upper surface of the test plate (i.e., measured by the thermocouple) during the ice-melting process, as revealed quantitatively in Fig. 6. With a reasonable assumption of having a uniform temperature distribution within the thin water film accumulated on the test surface, the energy conservation equation in the control volume during the initial ice-melting stage can be expressed as

$$\dot{Q}_{\text{cond}} + \dot{Q}_{\text{kin}} − \dot{Q}_{\text{conv}} − \dot{Q}_{\text{sub/evp}} = \dot{Q}_{\text{latent}} + \dot{Q}_{\text{ss−ice}} + \dot{Q}_{\text{ss−water}} + \dot{Q}_{\text{ss−water layer}} \quad (3)$$

where Q_{cond} is the conductive heat transfer term, Q_{kin} is the kinetic heating of the impinging ice particles, Q_{conv} is the convective heat taken by the airflow, Q_{sub} is the sublimation heat, Q_{evp} is the evaporation heat, Q_{latent} is the latent heat of fusion, and Q_{ss} is the sensible heat. As shown in Eq. (3), the thermal flux supplied by the electrical film heater and kinetic energy of the impinging ice particles will be dissipated by the convective heat transfer to the frozen-cold airflow, sublimation and evaporation, or absorbed as the latent heat of fusion associated with the melting of the impinged ice particles into liquid water and/or sensible heating change of the existing water layer.

Before having the airborne ice particles impinge onto the test surface, the conductive heat transfer input to the control volume will be dissipated only through the convective heat transfer to the frozen-cold airflow; therefore,

$$\dot{Q}_{\text{cond}} = \dot{Q}_{\text{conv}} = h_{\text{cv}} \cdot (T_{\text{surface−initial}} − T_\infty) \cdot A \quad (4)$$

where h_{cv} is the convective heat transfer coefficient, $T_{\text{surface−initial}}$ is the initial temperature of the test surface, T_∞ is the temperature of the incoming airflow, and A is the interface area within the control volume. The h_{cv} was measured by using a heat flux sensor for the test case of the present study, which was found to be about $0.43 \text{ kW/K} \cdot \text{m}^2$. Because the electrical film heater was operated to supply a constant thermal flux to the test plate, the conductive heat transfer supplied to the control volume was fixed as a constant value during the ice accretion experiment.

The impinging ice particles would introduce kinetic energy into the control volume, which can be expressed as

$$\dot{Q}_{\text{kin}} = \frac{1}{2}\dot{m}V\infty^2 \quad (5)$$

where the $\dot{m}$ is the mass flux of the impinged ice particles, which can be defined as $\dot{m} = \text{IWC} * V\infty * A$ where IWC is the ice water content in the incoming airflow and V_∞ is the freestream velocity of the incoming airflow.
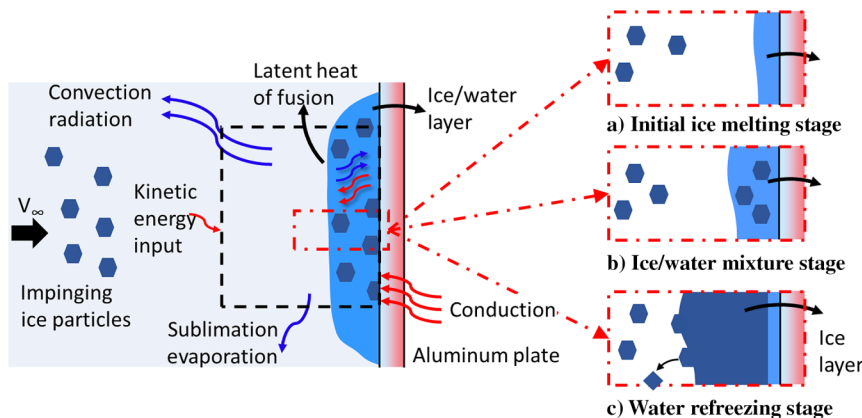

Fig. 7 A schematic for a theoretical analysis of the unsteady heat transfer characteristic over the heated test surface upon the impingement of the airborne ice particles.

The convective heat transfer occurs as the frozen-cold airflow impinged on the heated test surface. According to the heat transfer textbook of Incropera and DeWitt [43], the heat convection term in the energy equation can be expressed as

$$\dot{Q}_{\mathrm{conv}} = h_{\mathrm{cv}} \cdot (T(t) - T_\infty) \cdot A \tag{6}$$

where h_{cv} is the convective heat transfer coefficient, $T(t)$ is the water layer temperature as a function of with time, T_∞ is the temperature of the incoming airflow, and A is the area of the air/water interface within the control volume.

The heat in the control volume can also be transferred to the surroundings via evaporation and sublimation. As described in Dong et al. [44], the mass flux due to evaporation and sublimation can be usually estimated using

$$\dot{m}_{\mathrm{sub/evp}} = 0.696 \cdot \frac{h_{\mathrm{cv}}}{C_{\mathrm{air}}} \cdot \frac{p_s(T_{\mathrm{IR}}) - p_s(T_\infty)}{p_m} \cdot A \tag{7}$$

where the saturated vapor pressures $p_s(T_{\mathrm{IR}})$ and $p_s(T_\infty)$ can be obtained by following the work of Bartkus et al. [34]. T_{IR} is the water film temperature, and p_m is the average of wall pressure and free-stream pressure. Thus, the latent heat of evaporation and sublimation can be calculated by using the equation

$$\dot{Q}_{\mathrm{sub/evp}} = \dot{m}_{\mathrm{sub/evp}} \cdot L_w \tag{8}$$

where $\dot{m}_{\mathrm{sub/evp}}$ is the mass of evaporation and sublimation and L_w is the latent heat of sublimation of water.

The latent heat of fusion will be absorbed when the impinged ice particles are melting into liquid water after impinging onto the test surface. The total amount of the latent heat of fusion to be absorbed in the control volume is dependent on the mass of the melted ice particles. Within the control volume, ice mass is mainly coming from the impinged ice particles. The total amount of water layer accumulated inside the control volume is determined by the collection efficiency β, which is defined as the mass ratio of the melted ice particles to the total ice particles collected in the control volume. Therefore, the heat flux due to the absorption of the latent heat of fusion can be expressed as

$$\dot{Q}_{\mathrm{latent}} = \mathrm{IWC} \cdot V_\infty \cdot \beta \cdot A \cdot L_s \tag{9}$$

The sensible heat is mainly due to the enthalpy variations of melted ice particles from their initial temperature to water freezing temperature of $T_{\mathrm{water-freezing}} \approx 0.0°\mathrm{C}$, melted liquid water from 0°C to the surface temperature, which can be expressed as

$$\begin{aligned}
\dot{Q}_{\mathrm{ss}} &= \dot{Q}_{\mathrm{ss-ice}} + \dot{Q}_{\mathrm{ss-water}} + \dot{Q}_{\mathrm{ss-waterlayer}} \\
&= \mathrm{IWC} \cdot V_\infty \cdot \beta \cdot A \cdot C_i \cdot (0 - T_\infty) + \mathrm{IWC} \cdot V_\infty \cdot \beta \cdot A \\
&\quad \cdot (T(t) - 0) + (\mathrm{IWC} \cdot V_\infty \cdot \beta \cdot A \cdot t - \dot{m}_{\mathrm{run-out}}) \cdot \frac{dT(t)}{dt}
\end{aligned} \tag{10}$$

where C_i is the specific heat of ice and C_w is the specific heat of the water.

For the test cases of the present study, the kinetic energy and sublimation/evaporation heat (i.e., on the order of approximately 1 W/m^2) are usually several orders of magnitude smaller in comparison to the changes of other terms (i.e., on the order of approximately 10 kW/m^2) and thereby are negligible in the theoretical

analysis. Meanwhile, no melted water was found to flow away, indicating $\dot{m}_{\mathrm{run-out}} \approx 0$. By substituting Eqs. (4–10) into Eq. (3), the energy conservation equation can be rewritten as

$$\begin{aligned}
h_{\mathrm{cv}} \cdot (T_{\mathrm{surface-initial}} - T_\infty) - h_{\mathrm{cv}} \cdot (T(t) - T_\infty) &= \mathrm{IWC} \cdot V_\infty \cdot \beta \cdot L_s \\
&+ \mathrm{WC} \cdot V_\infty \cdot \beta \cdot A \cdot C_i \cdot (0 - T_\infty) \\
&+ \mathrm{IWC} \cdot V_\infty \cdot \beta \cdot (T(t) - 0) + \mathrm{IWC} \cdot V_\infty \cdot \beta \cdot t \cdot \frac{dT(t)}{dt}
\end{aligned} \tag{11}$$

Thus, the temperature change of the water film on the test surface as a function of time during the initial ice-melting stage can be derived based on the first-order differential of Eq. (11). Therefore, $T(t)$ can be expressed as

$$T(t) = \frac{C_1 \cdot t^{-\left(\frac{\beta \cdot IWC \cdot V_\infty \cdot c_w}{h_{cv} + \beta \cdot IWC \cdot V_\infty \cdot c_w}\right)} - h_{cv} T_{air} - \beta \cdot IWC \cdot v \cdot L_f - \beta \cdot IWC \cdot V_\infty \cdot c_i (0 - T_\infty)}{h_{cv} + \beta \cdot IWC \cdot V_\infty \cdot C_w} \tag{12}$$

where C_1 is a constant depending on the initial test conditions.

It should be noted that, based on Eq. (12), the theoretical prediction of the temperature of the water film over the test plate would reach infinity when the time t is close to zero. Therefore, the starting point for the theoretical prediction for the present study was chosen from the measured temperature value at the time instant of $t = 0.1$ s (i.e., $T_{t=0.1} \approx 9.7°\mathrm{C}$ for the test case of $T_p = +10°\mathrm{C}$). For theoretical prediction of the temperature evolution of the water film accreted on the test surface during the initial ice-melting stage, the collection efficiency β was the only unknown parameter in Eq. (12). By matching the starting condition of the theoretical prediction with the experimental result under the same test condition (e.g., assuming having the same temperature at the time of $t = 0.1$ s), the collection efficiency β can be estimated, which was found to be approximately 25% for the test case with $T_p = +10°\mathrm{C}$. Therefore, the temperature evolution of the water film on the test surface is predicted theoretically based on the Eq. (12) can be derived, which were plotted in Fig. 8. The measurement results of the IR thermal imaging system and the thermocouple mounted on the test surface are also plotted for a quantitative comparison. It can be seen clearly that the predictions
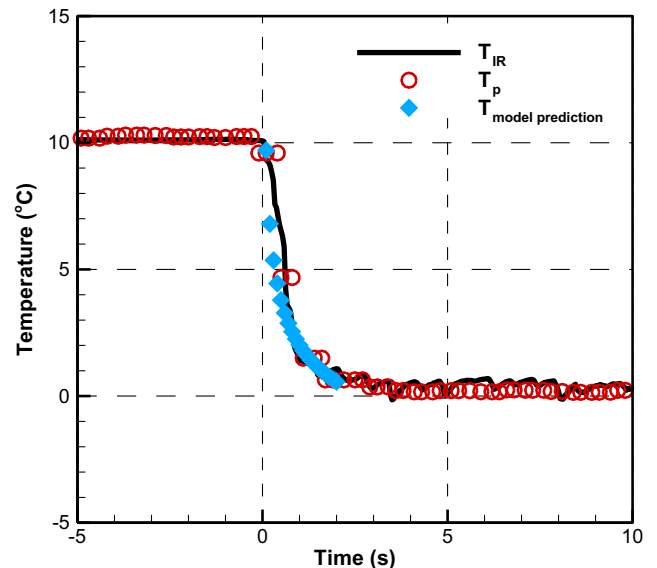

Fig. 8 The comparison of the theoretical prediction of the temperature of the water film on the test plate during the initial ice-melting stage against the measurement results for the test case with $T_p = +10°\mathrm{C}$.

based on Eq. (12) were found to agree with the measurement results well within the initial ice-melting stage of the ice accretion process.

With the same analysis procedure described previously, the collection efficiency of the impinged ice particles β during the initial ice-melting stage under other test conditions (i.e., for the test cases of $T_p = +20^\circ C$ and $T_p = +30^\circ C$) can also be determined by matching the starting values of the theoretical predictions with the corresponding measurement results. Figure 9 presents the estimated collection efficiency value β during the initial ice-melting stage of the ice accretion process as a function of the initial surface temperature of the test plate. The corresponding values of the collection efficiency of the impinged ice particles determined independently based on the measured growth rate of the water/ice layer thickness accreted on the test surface (i.e., based on the measurement data given in Fig. 3) were also given in Fig. 9 for a quantitative comparison. It can be seen clearly that the estimated values of the collection efficiency β based on the theoretical analysis described previously were found to agree reasonably well with those derived from the independently measured water/ice layer thickness on the test plate. It can also be seen that the collection efficiency value during the initial ice-melting stage increase almost linearly with the increasing surface temperature of the test plate. This is believed to be caused by the fact that the melting ratio of the impinged ice particles becomes greater as the temperature of the test plate increases, which will result in a thicker water film accumulating on the test surface. A thicker water film on the test surface would enable more impinged ice particles to stick on the test surface, hence a higher collection efficiency of the impinged ice particles on the test surface for the test case with a higher surface temperature of the test plate.

Figures 7b and 7c present the schematics for the heat transfer analysis during the water/ice mixture formation and water refreezing stages. As mentioned before, upon the impingement of airborne ice particles onto the heated test surface, the melting of the impinged ice particles caused the formation of a water layer accumulated on the test surface at the initial ice-melting stage. As time progressed, while more and more airborne ice particles impinged onto the test surface, fewer and fewer impinged ice particles were able to melt into liquid water due to the limited thermal flux supplied to the test plate. As a result, some impinged ice particles stayed as solid ice within the water film to form a water/ice mixture layer over the test surface. As shown in Fig. 6, the temperatures on both the outer and bottom surfaces of the water/ice mixture layer were found to stay almost constant around the water freezing temperature. Because no noticeable temperature variations were observed during the formation of a water/ice mixture layer on the test surface, no distinct ice melting and/or water freezing was believed to take place in the water/ice mixture formation stage.

Because the water/ice mixture layer accreted on the test plate was exposed to frozen-cold impinging airflow, intensive convective heat transfer would cause the dissipation of the thermal flux from the water/ice mixture layer to the frozen-cold airflow. With continuous impingement of the airborne ice particles on the water/ice mixture layer, the thickness of the water/ice mixture layer was found to grow monotonically, as revealed in Fig. 3. The thicker water/ice mixture layer induced a greater thermal resistance to the heat conduction from the heated test surface to the outer surface of the water/ice mixture layer accreted on the test surface. With the increasing thickness of the water/ice mixture layer accreted on the test surface, less thermal flux supplied by the electrical film heater to the test plate was dissipated from the outer surface of the water/ice mixture layer. Therefore, while the temperature at the bottom surface of the water/ice mixture layer (i.e., the temperature measured by the thermocouple mounted on the test plate) was found to stay constant at the water freezing temperature during the entire ice accretion process, the temperature on the outer surface of the water/ice layer was found to decrease monotonically as the time progresses.

With the temperature of the water/ice layer becoming lower than the water freezing temperature, the liquid water in the water/ice mixture layer started to freeze into solid ice. This indicates that the icing process will transit from the water/ice mixture stage into the water refreezing stage, resulting in a solid ice layer with a rigid outer surface accreted on the test surface. As shown schematically in Fig. 7c, the growth of the solid ice layer accreted over the test surface would be mainly due to the erosion caused by the continuous impingement of airborne ice particles. Because of the intensive convective heat transfer with the frozen-cold airflow, the temperature on the upper surface of the ice layer accreted on the test plate was found to decrease continuously as time progresses. However, the surface temperature of the test plate (i.e., on the bottom surface of the accreted ice layer) was still found to stay almost unchanged at water freezing temperature during the entire icing process. It suggests that a thermal balance was reached; i.e., the thermal flux provided by the electric film heater to the test plate was balanced by the heat conduction from the bottom surface of the ice layer to its outer surface. The supplied thermal flux was dissipated eventually by the frozen-cold airflow via intensive convective heat transfer over the outer surface of the accreted ice layer on the test plate.

It should also be noted that, due to the substantially higher thermal flux supplied for the test case of $T_p = +30^\circ C$, the temperatures on both outer and bottom surfaces of the water/ice layer accreted over the test surface were found to be always above the water freezing temperature (i.e., $T_{surface} > 0.0^\circ C$), as shown in Fig. 6c. This indicates that the higher thermal flux supplied to the test plate prevented the liquid water in the water/ice layer from refreezing into solid ice. Therefore, a flowable water/ice mixture layer was found to exist on the test surface during the entire icing experiment for the test case with $T_p = +30^\circ C$, as revealed from the acquired images given in Fig. 2d.

IV. Conclusions

In the present study, a comprehensive experimental investigation was conducted to examine the dynamic ice accretion process upon the impingement of airborne ice particles/crystals onto a heated test surface pertinent to aeroengine icing phenomena. The experimental study was performed by leveraging a specially designed ice crystal icing test facility situated in a walk-in freezing chamber with the environment temperature controllable down to $-10.0^\circ C$. Microsized, ice particles were generated and injected into a wind tunnel at a controllable amount to form airborne ice particles and then forced to impinge onto a test plate at the impacting speed at 40 m/s. A test plate, which was made of aluminum with a high thermal conductivity, was heated up by using an electric film heater with different supplied power inputs to adjust the surface temperature of the test plate for different test conditions. During the experiments, while high-resolution imaging systems were used to record the dynamic ice accretion process on the heated test surface from different perspectives, a high-speed imaging system equipped with a 60X microscopic objective acquires images at the frame up to 10 KHz to examine the impinging characteristics of the ice
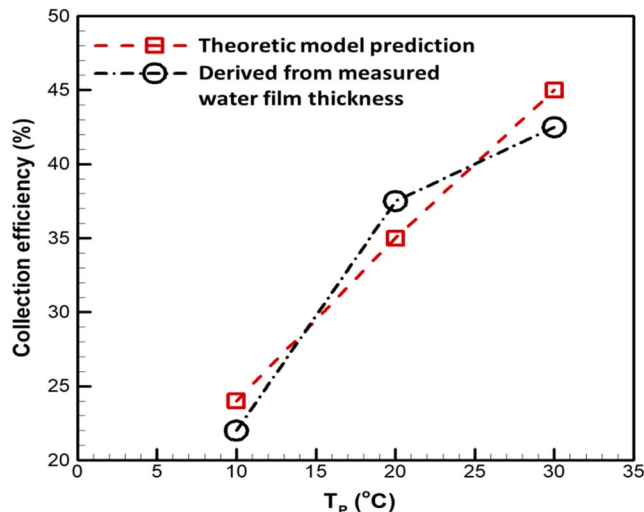

Fig. 9 The theoretically predicted collection efficiency of the impinging ice particles against those derived from the water film thickness measurements.

particles at the initial stage of ice accretion process. In addition to using a high-speed IR thermal imaging system to characterize the time evolution of the temperature distributions on the surface of the water/ice layer accreted on the test surface, a thermocouple was also flush mounted on the surface of the test plate quantify the unsteady heat transfer characteristics during the dynamic ice accretion process.

It was revealed clearly that, upon the impingement of airborne ice particles onto the heated test surface, the ice accretion process can be divided into three distinct stages, i.e., 1) an ice-melting stage at the beginning, followed by 2) a water/ice mixture formation stage, and then 3) a water refreezing stage, resulting in the formation of an ice layer accreted on the heated test surface. At the initial ice-melting stage, a portion of the impinged ice particles was found to melt into liquid water rapidly upon impinging onto the heated test surface, resulting in a layer of water film that accumulated on the test surface. The absorption of the latent heat of fusion associated with the liquefaction process caused a rapid drop of the test surface temperature down to the water freezing temperature. Because of the presence of the water film layer on the test surface, the impinged ice particles were found to become more readily to stick to the wetted test surface, instead of bouncing off from the test surface. With continuous impingement of airborne ice particles, fewer and fewer impinged ice particles were found to be able to melt into liquid water due to the limited thermal flux supplied to the test plate to balance out the required latent heat of fusion associated with the liquefaction process, resulting in the formation of a water/ice mixture layer accreted on the heated test surface. During the water/ice mixture formation stage, while the thickness of the water/ice mixture layer accreted on the test surface was found to increase almost linearly as the time progressed, the temperature of the water/ice mixture layer was found to stay almost unchanged near the water freezing temperature. Because of the intensive convective heat transfer with the frozen-cold incoming airflow, the temperature on the outer surface of the water/ice mixture layer was found to decrease gradually and become lower than the water freezing temperature eventually. As a result, the liquid water in the water/ice mixture layer was found refreeze into solid ice (i.e., transition into water refreezing stage), causing the formation of a solid ice layer accreted over the test surface eventually.

The high-speed microscopic imaging results uncovered many interesting characteristics about the impingement of airborne ice particles onto frozen-cold and heated test surfaces. Upon impinging onto the test plate at the impacting speed, while small ice particles in spherical shapes (i.e., with their MVD being smaller than 100 μm for the present study) were found to be more likely to fully bounce off from the test plate with almost no impingement residues remaining on the test surface. However, large, nonspheric ice particles (i.e., with their MVD being greater than 200 μm) were found to experience a catastrophic fragmentation process to break up into many smaller pieces with noticeable amount of impingement residues remaining on the test surface. It was also found that the presence of a liquid water film from the melting of the impacted ice particles on the heated test surface will be very beneficial to enable more impinged ice particles to stay stuck on the test surface, causing a much faster growth of the water/ice layer accreted on the test surface.

Acknowledgments

References

[1] Bragg, M. B., Broeren, A. P., and Blumenthal, L. A., "Iced-Airfoil Aerodynamics," *Progress in Aerospace Sciences*, Vol. 41, No. 5, 2005, pp. 323–362.
https://doi.org/10.1016/j.paerosci.2005.07.001

[2] Gao, L., Liu, Y., Zhou, W., and Hu, H., "An Experimental Study on the Aerodynamic Performance Degradation of a Wind Turbine Blade Model Induced by Ice Accretion Process," *Renewable Energy*, Vol. 133, April 2019, pp. 663–675.
https://doi.org/10.1016/J.RENENE.2018.10.032

[3] Cao, Y., Tan, W., and Wu, Z., "Aircraft Icing: An Ongoing Threat to Aviation Safety," *Aerospace Science and Technology*, Vol. 75, April 2018, pp. 353–385.
https://doi.org/10.1016/j.ast.2017.12.028

[4] Li, L., Liu, Y., and Hu, H., "An Experimental Study on Dynamic Ice Accretion Process over the Surfaces of Rotating Aero-Engine Spinners," *Experimental Thermal and Fluid Science*, Vol. 109, Dec. 2019, Paper 109879.
https://doi.org/10.1016/J.EXPTHERMFLUSCI.2019.109879

[5] Tian, L., Li, L., Hu, H., and Hu, H., "Experimental Study of Dynamic Ice Accretion Process over Rotating Aeroengine Fan Blades," *Journal of Thermophysics and Heat Transfer*, 2022, pp. 1–12.
https://doi.org/10.2514/1.T6667

[6] Dong, W., Zhu, J., Zheng, M., Lei, G. L., and Zhou, Z. X., "Experimental Study on Icing and Anti-Icing Characteristics of Engine Inlet Guide Vanes," *Journal of Propulsion and Power*, Vol. 31, No. 5, 2015, pp. 1330–1337.
https://doi.org/10.2514/1.B35679

[7] Li, L., Liu, Y., Tian, L., Hu, H., Hu, H., Liu, X., Hogate, I., and Kohli, A., "An Experimental Study on a Hot-Air-Based Anti-/De-Icing System for Aero-Engine Inlet Guide Vanes," *Applied Thermal Engineering*, Vol. 167, Feb. 2020, Paper 114778.
https://doi.org/10.1016/j.applthermaleng.2019.114778

[8] Kissling, H., "Aircraft Engine Anti-Icing Test and Evaluation Technology," AIAA Paper 1972-0162, 1972.
https://doi.org/10.2514/6.1972-162

[9] Al-Khalil, K. M., Keith, T. G., Dewitt, K. J., Nathman, J. K., and Dietrich, D. A., "Thermal Analysis of Engine Inlet Anti-Icing Systems," *Journal of Propulsion and Power*, Vol. 6, No. 5, 1990, pp. 628–634.
https://doi.org/10.2514/3.23264

[10] Flegel, A. B., "Ice Crystal Icing Research at NASA Glenn Research Center," *9th AIAA Atmospheric and Space Environments Conference*, AIAA Paper 2017-40185, 2017.
https://doi.org/10.2514/6.2017-4085

[11] Struk, P. M., Bartkus, T. P., Bencic, T. J., King, M. C., Ratvasky, T. P., van Zante, J. F., and Tsao, J. C., "An Initial Study of the Fundamentals of Ice Crystal Icing Physics in the NASA Propulsion Systems Laboratory," *9th AIAA Atmospheric and Space Environments Conference*, AIAA Paper 2017-4242, 2017.
https://doi.org/10.2514/6.2017-4242

[12] Mason, J., Strapp, W., and Chow, P., "The Ice Particle Threat to Engines in Flight," *44th AIAA Aerospace Sciences Meeting and Exhibit*, AIAA Paper 2006-0206, Jan. 2006.
https://doi.org/10.2514/6.2006-206

[13] Bravin, M., Strapp, J., and Mason, J., "An Investigation into Location and Convective Lifecycle Trends in an Ice Crystal Icing Engine Event Database," SAE TP 2015-01-2130, 2015.
https://doi.org/10.4271/2015-01-2130

[14] Liu, Y., Kolbakir, C., Hu, H., and Hu, H., "A Comparison Study on the Thermal Effects in DBD Plasma Actuation and Electrical Heating for Aircraft Icing Mitigation," *International Journal of Heat and Mass Transfer*, Vol. 124, Sept. 2018, pp. 319–330.
https://doi.org/10.1016/j.ijheatmasstransfer.2018.03.076

[15] Fortin, G., Laforte, J. L., and Ilinca, A., "Heat and Mass Transfer During Ice Accretion on Aircraft Wings with an Improved Roughness Model," *International Journal of Thermal Sciences*, Vol. 45, No. 6, 2006, pp. 595–606.
https://doi.org/10.1016/j.ijthermalsci.2005.07.006

[16] Liu, Y., and Hu, H., "An Experimental Investigation on the Unsteady Heat Transfer Process over an Ice Accreting Airfoil Surface," *International Journal of Heat and Mass Transfer*, Vol. 122, July 2018, pp. 707–718.
https://doi.org/10.1016/j.ijheatmasstransfer.2018.02.023

[17] Liu, Y., Zhang, K., Tian, W., and Hu, H., "An Experimental Investigation on the Dynamic Ice Accretion and Unsteady Heat Transfer over an Airfoil Surface with Embedded Initial Ice Roughness," *International Journal of Heat and Mass Transfer*, Vol. 146, Jan. 2020, Paper 118900.
https://doi.org/10.1016/j.ijheatmasstransfer.2019.118900

[18] Baumert, A., Bansmer, S., Trontin, P., and Villedieu, P., "Experimental and Numerical Investigations on Aircraft Icing at Mixed Phase Conditions," *International Journal of Heat and Mass Transfer*, Vol. 123, Aug. 2018, pp. 957–978.
https://doi.org/10.1016/j.ijheatmasstransfer.2018.02.008

[19] Zhang, R., Hao, P., Zhang, X., and He, F., "Supercooled Water Droplet Impact on Superhydrophobic Surfaces with Various Roughness and Temperature," *International Journal of Heat and Mass Transfer*,

Vol. 122, July 2018, pp. 395–402.
https://doi.org/10.1016/j.ijheatmasstransfer.2018.01.076

[20] Reddy, E., Abumeri, G., Murthy, P., and Chamis, C., "Structural Tailoring of Aircraft Engine Blade Subject to Ice Impact Constraints," *4th Symposium on Multidisciplinary Analysis and Optimization*, AIAA Paper 1992-4710, Sept. 1992.
https://doi.org/10.2514/6.1992-4710

[21] Yuter, S. E., Houze, R. A., Smith, E. A., Wilheit, T. T., and Zipser, E., "Physical Characterization of Tropical Oceanic Convection Observed in KWAJEX," *Journal of Applied Meteorology*, Vol. 44, No. 4, 2005, pp. 385–415.
https://doi.org/10.1175/JAM2206.1

[22] Leroy, D., Fontaine, E., Schwarzenboeck, A., and Strapp, J. W., "Ice Crystal Sizes in High Ice Water Content Clouds. Part I: On the Computation of Median Mass Diameter from In Situ Measurements," *Journal of Atmospheric and Oceanic Technology*, Vol. 33, No. 11, 2016, pp. 2461–2476.
https://doi.org/10.1175/JTECH-D-15-0151.1

[23] Leroy, D., Fontaine, E., Schwarzenboeck, A., Strapp, J. W., Korolev, A., McFarquhar, G., Dupuy, R., Gourbeyre, C., Lilie, L., Protat, A., Delanoe, J., Dezitter, F., and Grandin, A., "Ice Crystal Sizes in High Ice Water Content Clouds. Part II: Statistics of Mass Diameter Percentiles in Tropical Convection Observed During the HAIC/HIWC Project," *Journal of Atmospheric and Oceanic Technology*, Vol. 34, No. 1, 2017, pp. 117–136.
https://doi.org/10.1175/JTECH-D-15-0246.1

[24] Heymsfield, A. J., Bansemer, A., Field, P. R., Durden, S. L., Stith, J. L., Dye, J. E., Hall, W., and Grainger, C. A., "Observations and Parameterizations of Particle Size Distributions in Deep Tropical Cirrus and Stratiform Precipitating Clouds: Results from In Situ Observations in TRMM Field Campaigns," *Journal of the Atmospheric Sciences*, Vol. 59, No. 24, 2002, pp. 3457–3491.
https://doi.org/10.1175/1520-0469(2002)059<3457:OAPOPS>2.0.CO;2

[25] Yuter, S. E., Houze, R. A., Smith, E. A., Wilheit, T. T., Zipser, E., and Yuter, S., "Physical Characterization of Tropical Oceanic Convection Observed in KWAJEX," *Journal of Applied Meteorology and Climatology*, Vol. 44, No. 4, 2005, pp. 385–415.

[26] MacLeod, J., and Fuleki, D., "Ice Crystal Accretion Test Rig Development for a Compressor Transition Duct," *AIAA Atmospheric and Space Environments Conference*, AIAA Paper 2010-7259, Aug. 2010, pp. 1–9.
https://doi.org/10.2514/6.2010-7529

[27] Van Zante, J., Ide, R., and Steen, L.-C., "NASA Glenn Icing Research Tunnel: 2014 Cloud Calibration Procedure and Results," *4th AIAA Atmospheric and Space Environments Conference*, AIAA Paper 2012-2933, 2012.
https://doi.org/10.2514/6.2012-2933

[28] Struk, P. M., Bencic, T., Tsao, J.-C., Fuleki, D., and Knezevici, D. C., "Preparation for Scaling Studies of Ice-Crystal Icing at the NRC Research Altitude Test Facility," *5th AIAA Atmospheric and Space Environments Conference*, AIAA Paper 2013-2675, 2013.
https://doi.org/10.2514/6.2013-2675

[29] Struk, P. M., Ratvasky, T. P., Bencic, T. J., Van Zante, J. F., King, M. C., Tsao, J.-C., and Bartkus, T. P., "An Initial Study of the Fundamentals of Ice Crystal Icing Physics in the NASA Propulsion Systems Laboratory," AIAA Paper 2017-4242, June 2017, pp. 11–2.
https://doi.org/10.2514/6.2017-4242

[30] Currie, T. C., Fuleki, D., and Mahallati, A., "Experimental Studies of Mixed-Phase Sticking Efficiency for Ice Crystal Accretion in Jet Engines," *6th AIAA Atmospheric and Space Environments Conference*,

[31] Currie, T., Fuleki, D., and Davison, C., "Simulation of Ice Particle Melting in the NRCC RATFac Mixed-Phase Icing Tunnel," SAE TP 2015-01-2107, 2015.
https://doi.org/10.4271/2015-01-2107

[32] Tsao, J. C., Struk, P., and Oliver, M., "Possible Mechanisms for Turbofan Engine Ice Crystal Icing at High Altitude," *6th AIAA Atmospheric and Space Environments Conference*, AIAA Paper 2014-3044, June 2014.

[33] Struk, P. M., King, M. C., Bartkus, T. P., Tsao, J.-C., Fuleki, D., Neuteboom, M., and Chalmers, J., "Ice Crystal Icing Physics Study Using a NACA 0012 Airfoil at the National Research Council of Canada's Research Altitude Test Facility," *2018 Atmospheric and Space Environments Conference*, AIAA Paper 2018-4224, 2018.
https://doi.org/10.2514/6.2018-4224

[34] Bartkus, T., Tsao, J., and Struk, P., "Analysis of Experimental Ice Accretion Data and Assessment of a Thermodynamic Model During Ice Crystal Icing," SAE TP 2019-01-2016, 2019.
https://doi.org/10.4271/2019-01-2016

[35] Currie, T. C., and Fuleki, D., "Experimental Results for Ice Crystal Icing on Hemispherical and Double Wedge Geometries at Varying Mach Numbers and Wet Bulb Temperatures," *8th AIAA Atmospheric and Space Environments Conference*, AIAA Paper 2016-3740, June 2016, pp. 1–22.
https://doi.org/10.2514/6.2016-3740

[36] MacLeod, J., "Development of Ice Crystal Facilities for Engine Testing," SAE TP 2007-01-3290, 2007.
https://doi.org/10.4271/2007-01-3290

[37] Bucknell, A., McGilvray, M., Gillespie, D. R. H., Jones, G., Reed, A., and Buttsworth, D. R., "Heat Transfer in the Core Compressor Under Ice Crystal Icing Conditions," *Journal of Engineering for Gas Turbines and Power*, Vol. 140, No. 7, 2018, pp. 1–13.
https://doi.org/10.1115/1.4038460

[38] Hauk, T., Bonaccurso, E., Roisman, I. V., and Tropea, C., "Ice Crystal Impact onto a Dry Solid Wall. Particle Fragmentation," *Proceedings of the Royal Society A: Mathematical, Physical and Engineering Sciences*, Vol. 471, No. 2181, 2015, Paper 20150399.
https://doi.org/10.1098/rspa.2015.0399

[39] Hauk, T., "Investigation of the Impact and Melting Process of Ice Particles," Ph.D. Thesis, Technical Univ. of Darmstadt, Darmstadt, Germany, 2016.

[40] Incropera, F. P., and Dewitt, D., *Introduction to Heat Transfer*, Wiley, New York, 2002, p. 899.

[41] Waldman, R. M., and Hu, H., "High-Speed Imaging to Quantify Transient Ice Accretion Process over an Airfoil," *Journal of Aircraft*, Vol. 53, No. 2, 2016, pp. 369–377.
https://doi.org/10.2514/1.C033367

[42] Liu, Y., Li, L., Ning, Z., Tian, W., and Hu, H., "Experimental Investigation on the Dynamic Icing Process over a Rotating Propeller Model," *Journal of Power and Propulsion*, Vol. 34, No. 4, 2018, pp. 1–15.
https://doi.org/10.2514/1.B36748

[43] Incropera, F. P., and DeWitt, D. P., *Fundamentals of Heat and Mass Transfer*, Wiley, New York, 1996, p. 347.

[44] Dong, W., Zhu, J., Zheng, M., and Chen, Y., "Thermal Analysis and Testing of Nonrotating Cone with Hot-Air Anti-Icing System," *Journal of Propulsion and Power*, Vol. 31, No. 3, 2015, pp. 896–903.
https://doi.org/10.2514/1.B35378

D. Zhao
Associate Editor